ACS Catalysis

pubs.acs.org/acscatalysis

Research Article

# *Operando* Identification of the Reversible Skin Layer on $Co_3O_4$ as a Three-Dimensional Reaction Zone for Oxygen Evolution

Tim Wiegmann, Ivan Pacheco, Finn Reikowski, Jochim Stettner, Canrong Qiu, Mathilde Bouvier, Manon Bertram, Firas Faisal, Olaf Brummel, Jörg Libuda, Jakub Drnec, Philippe Allongue,* Fouad Maroun,* and Olaf M. Magnussen*

Cite This: *ACS Catal.* 2022, 12, 3256−3268

Read Online

ACCESS | Metrics & More | Article Recommendations | Supporting Information

**ABSTRACT:** Co oxides and oxyhydroxides have been studied extensively in the past as promising electrocatalysts for the oxygen evolution reaction (OER) in neutral to alkaline media. Earlier studies showed the formation of an ultrathin $CoO_x(OH)_y$ skin layer on $Co_3O_4$ at potentials above 1.15 V vs reversible hydrogen electrode (RHE), but the precise influence of this skin layer on the OER reactivity is still under debate. We present here a systematic study of epitaxial spinel-type $Co_3O_4$ films with defined (111) orientation, prepared on different substrates by electrodeposition or physical vapor deposition. The OER overpotential of these samples may vary up to 120 mV, corresponding to two orders of magnitude differences in current density, which cannot be accounted for by differences in the electrochemically active surface area. We demonstrate by a careful analysis of *operando* surface X-ray diffraction measurements that these differences are clearly correlated with the average thickness of the skin layer. The OER reactivity increases with the amount of formed skin layer, indicating that the entire three-dimensional skin layer is an OER-active interphase. Furthermore, a scaling relationship between the reaction centers in the skin layer and the OER activity is established. It suggests that two lattice sites are involved in the OER mechanism.

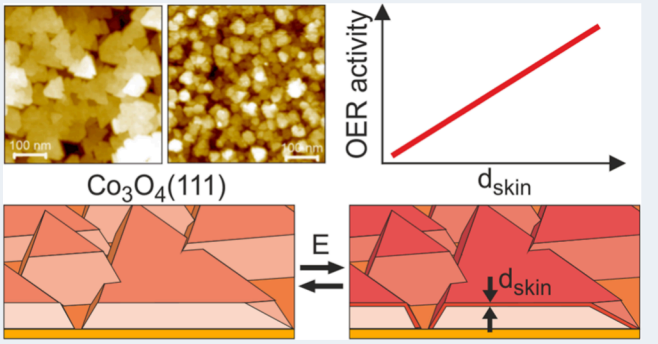


**KEYWORDS:** *Co oxide, electrocatalysis, oxygen evolution reaction, surface restructuring, structure−activity relationship, surface X-ray diffraction, model catalysts*



## 1. INTRODUCTION

The search for commercially viable catalysts for the oxygen evolution reaction (OER), which is the bottleneck for electrochemical water splitting, is a key challenge in the worldwide transition to a renewable-based energy system. Earth-abundant catalysts in general and cobalt (hydro-)oxides in particular are of great interest. The latter show promising catalytic properties and are stable in alkaline and neutral electrolytes under ambient conditions. Moreover, they may be synthesized with a great variety of morphologies (nanosheets, particles, or thin films) and with a crystalline or amorphous structure. Preparation methods include solvothermal,[1−3] photochemical,[4] and electrochemical[5−7] syntheses as well as deposition under vacuum conditions.[8−11] Especially the mixed-valence $Co_3O_4$ spinel has been extensively studied and may be considered as a prototypical OER oxide catalyst.[2,3,5−10,12−48] In many cases, the precise surface structure and electrochemically active surface area (ECSA) of the catalysts are unknown or poorly defined, however. Thus, the comparison of the electrocatalytic activity of different catalysts is difficult.

A further challenge in understanding the OER on earth-abundant catalysts is characterizing the influence of the surface structure on the catalyst's reactivity. Many of these materials undergo surface restructuring at the strongly oxidizing potentials where the OER occurs (for recent reviews, see refs 49−52). Here, the surface of the catalyst is typically converted into an oxide in which the metal cations shift to a higher oxidation state, which is considered to be more electrochemically active. In the case of $Co_3O_4$, the OER occurs on a subnanometer skin layer composed of X-ray-amorphous $CoO_x(OH)_y$ (i.e., a phase that does not contain sufficiently crystalline regions to produce measurable Bragg peaks) and not on the surface of the bulk $Co_3O_4$ spinel structure.[2,3,7] In contrast to many other systems, this skin layer is converted back into crystalline $Co_3O_4$ by reversing the electrode potential. This reversible skin layer formation was first

Received: November 10, 2021
Revised: January 6, 2022

observed on polycrystalline samples by Bergmann et al. and was believed to be promoted by the OER.[2,3] However, our group showed that the skin layer forms gradually at potentials above 1.15 $V_{RHE}$, i.e., close to the thermodynamic equilibrium potential of the $Co_3O_4$/CoOOH phase transition, and well before the onset of the OER, by *operando* surface X-ray diffraction (SXRD) studies of epitaxial $Co_3O_4$ thin-film electrodes.[7] The skin layer thus has to be attributed to the oxide electrochemistry itself, and this explains its reversible formation and back-crystallization with potential.

The structural complexity of the oxide/electrolyte interface structure probably explains why the OER mechanism on cobalt oxide is still under debate despite extensive atomic-scale studies, including *in situ* spectroscopic studies[8,24,41,42,45,53] and theoretical studies by density functional theory (DFT).[20,21,29,32−35,54−56] Studies by X-ray absorption spectroscopy (XAS), X-ray photoelectron spectroscopy, and Raman spectroscopy indicated an overall increase in the Co oxidation state under OER conditions and attributed the high electrocatalytic activity to those species.[24,41,42,45,53] However, these measurements do not enable determination of the precise location and amount of these OER-active Co species. Most studies assume that they are restricted to the oxide surface, but in some cases, it was suggested that all Co centers in the oxide contribute.[57,58] Furthermore, OER mechanisms involving one as well as two sites have been proposed.

In the above experimental studies, the OER activity of $Co_3O_4$ is qualitatively linked with the increased Co oxidation state and the associated coordination changes at the oxide surface, from which the identification of the active site was attempted.[2,3] However, the dependence of the electrocatalyst properties on the spatial extension of the transformed surface region, i.e., the effective surface density of active sites, has not been determined yet. Also, in *ab initio* theory studies of $Co_3O_4$ catalysts, only crystalline surfaces were considered up to now and thus did not allow conclusions on the role of the skin layer.[20,29,32−35,54]

In this work, we derive a quantitative relationship between the amount of formed skin layer and the OER activity. To achieve this, we performed systematic comparative studies by atomic force microscopy (AFM), *operando* SXRD, and electrochemical measurements of well-defined spinel-type $Co_3O_4$ epitaxial films with an identical (111) surface orientation and similar microscopic oxide surface area. These include films deposited on Ir(100) by physical vapor deposition (PVD) under ultrahigh vacuum (UHV) conditions and electrodeposited films on Au(111), Au(100), or CoOOH(001). We present simultaneously obtained electrocatalytic and *operando* structural data of these samples and correlate those quantitatively. All samples exhibit reversible potential-dependent changes in grain size and strain in the pre-OER regime, which are assigned to the formation of the skin layer. Our data clearly show that the average thickness of this skin layer, which varies strongly with the sample type, has a pronounced impact on the OER activity. A quantitative relationship between the skin layer volume and the electrocatalytic properties is established, which implies that the entire skin layer is a three-dimensional OER-active region. In addition, we discuss this structure−reactivity relationship to estimate a turn-over frequency (TOF) and provide insight into the number of sites involved in the reaction.

## 2. EXPERIMENTAL SECTION

**2.1. Preparation of $Co_3O_4$(111) Films on Ir(100).** Deposition of $Co_3O_4$ on Ir(100) was performed by physical vapor deposition (PVD) under UHV conditions,[8,9] using a procedure adapted from the method of Heinz and co-workers.[59,60] Initially, the disc-shaped Ir(100) single crystal (Surface Preparation Laboratory, 99.995%, depth of roughness <0.03 $\mu$m, accuracy of orientation <0.1°) was cleaned by $Ar^+$ bombardment (Linde 6.0, $9 \times 10^{-5}$ mbar, 1.8 keV, 300 K) and several annealing cycles (UHV, 1123 K, 5 min; followed by annealing in $O_2$, Linde 5.0, $5 \times 10^{-8}$ mbar, 1123 K). Flashing the sample to 1123 K in UHV yielded the Ir(100)-(5×1) reconstructed surface. Following this, successive flashing of the surface to 873 K in an $O_2$ atmosphere ($5 \times 10^{-8}$ mbar) and cooling to 393 K in $O_2$ yielded the Ir(100)-(2×1)O reconstructed surface, which was confirmed by LEED. On this substrate, cobalt (Alfa Aesar, 99.95%, 2 mm rod) was then deposited in a reactive $O_2$ atmosphere ($8 \times 10^{-6}$ mbar) at temperatures between 243 and 300 K to avoid the initial adsorption of water, with the evaporation rate calibrated by a quartz crystal microbalance. The evaporation time was adjusted to yield films of 15 nm thickness. An ordered film was formed by annealing in $O_2$ ($5 \times 10^{-7}$ mbar) at 523 K for 3 min, at 698 K for 5 min ($1 \times 10^{-7}$ mbar), and finally in UHV at 698 K for 3 min. The successful preparation of (111)-oriented $Co_3O_4$ was confirmed by LEED, which revealed the typical diffraction pattern of the spinel structure.

**2.2. Preparation of $Co_3O_4$(111) films on Au(100), Au(111), and CoOOH(001).** Electrodeposition (ED) of $Co_3O_4$ on Au(100) and Au(111) was performed on hat-shaped single crystals (MaTecK, accuracy of orientation <0.1°), which were initially cleaned for 1 min in a hot 1:2 mixture of 30% $H_2O_2$ and 96% $H_2SO_4$ (both Carlo Erba, RSE) and then flame-annealed for 5 min using a butane torch. Oxide deposition was performed in an aqueous, oxygen-free solution of 1 mM $Co(NO_3)_2$ + 1.2 mM sodium tartrate (tart) + $x$ M NaOH, with either $x = 1$ or $x = 2$ prepared from high-purity Co nitrate (Merck, >99.0%), Na tartrate (Sigma-Aldrich, ACS reagent, >99.5%), NaOH (Merck, ACS reagent, Fe content <0.0005%), and Milli-Q water. Oxide deposition was performed at reflux temperature (~103 °C) at a constant potential of -0.55 V vs a mercury sulfate reference electrode, where the Co(II) complex is oxidized and Co(III) precipitates on the electrode surface.[5,6] A charge density of 8 mC $cm^{-2}$ was passed to grow $Co_3O_4$ films with (111) orientation of 15−25 nm thickness. After deposition, the samples were removed from the reflux cell, rinsed with ultrapure water, and dried with Ar. For $Co_3O_4$ deposition on CoOOH(001), an atomically smooth CoOOH(001) layer was first electrodeposited on Au(111) in a 5 M NaOH Co tartrate solution at reflux temperature as described in ref 7. The sample was removed from the reflux cell, rinsed with ultrapure water, and dried with Ar before use for the deposition of the $Co_3O_4$ film on top.

**2.3. *Ex Situ* AFM Characterization of the Samples.** The morphology of the samples was characterized with atomic force microscopy (Agilent PicoPlus) in a $N_2$ atmosphere using the tapping mode. Silicon AFM tips with a cantilever oscillating frequency of ~190 kHz ($\mu$masch) were used. For each sample, different regions of the samples (at distances of ~1 mm) were imaged to ensure that the observed morphology was representative of the sample morphology. The measured images allowed us to obtain the Co oxide coverage and


https://doi.org/10.1021/acscatal.1c05169
ACS Catal. 2022, 12, 3256−3268

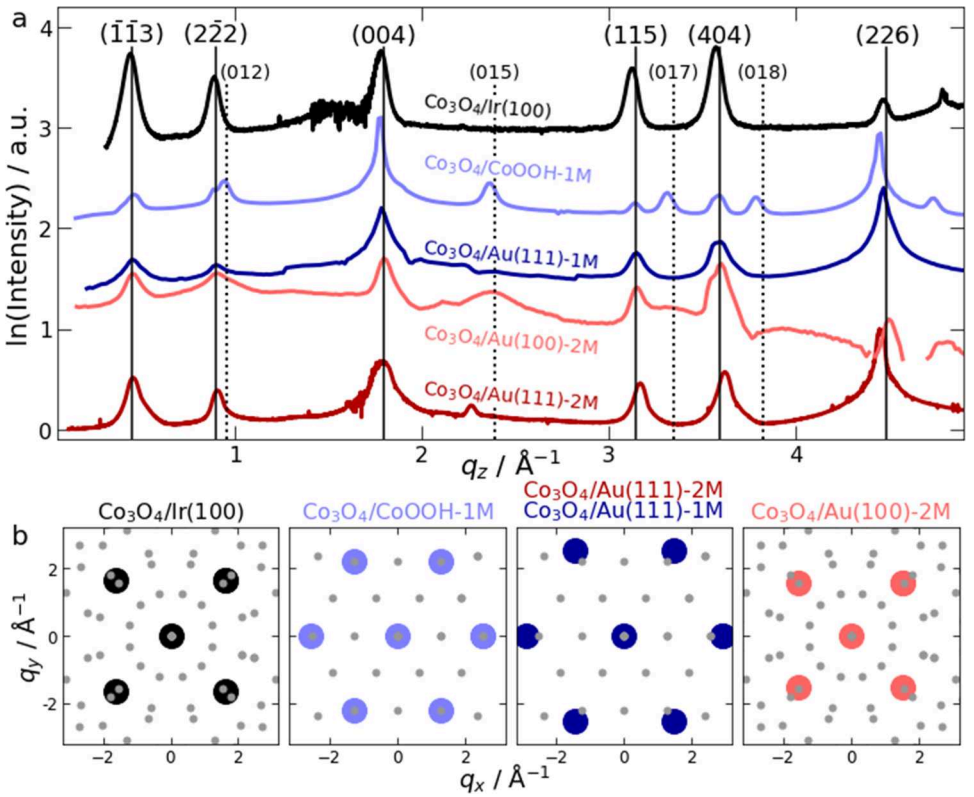


**Figure 1.** SXRD results on the structure and epitaxial arrangement of the five samples. (a) Crystal truncation rods at $q_{inplane}$ = 2.5385 Å$^{-1}$, the in-plane scattering vector of the $Co_3O_4$(404) peak. Intensities are displayed on alogarithmic scale and with a vertical offset between different samples. Positions of $Co_3O_4$ peaks along the rods are marked with solid lines and indexed according to the $Co_3O_4$ simple cubic unit cell. Positions of CoOOH peaks are marked with dotted lines and indexed according to the CoOOH hexagonal unit cell. (b) Schematic in-plane diffraction patterns of the five samples, derived from reciprocal space surveys, that illustrate the epitaxial arrangements. The positions of $Co_3O_4$ and substrate CTRs are indicated by gray and colored circles, respectively.

roughness. Since the films are composed of tightly packed islands, the film roughness obtained by AFM depends on the tip sharpness and may be underestimated.

**2.4. *Operando* SXRD Experiments.** *Operando* SXRD studies employed the same methodology as in our previous study[7] (see Supporting Information, Section S1 for details) and were performed at two different surface diffraction beamlines: (i) at ESRF beamline ID03 (photon energy 22.5 keV, photon flux 4 × 10$^{11}$ counts/s, beam size 250 $\mu$m width × 30 $\mu$m height) and (ii) at PETRA III beamline P23 (photon energy 18.7 or 22.5 keV, photon flux 5 × 10$^{11}$ counts/s, beam size 200 $\mu$m width × 30 $\mu$m height). All measurements were performed in a six-circle geometry and at a fixed grazing incidence angle of 0.34°.

During the measurements, the samples were kept in an electrochemical cell specifically designed for *operando* SXRD studies.[7] For the samples on Au substrates, the cell was made from PEEK, with a PTFE seal fitted tightly around the hat-shaped sample to expose only the polished top part with the epitaxial $Co_3O_4$ film to the electrolyte. Imperfect sealing can result in partial penetration of the electrolyte into the gap between the PTFE seal and the crystal wall, resulting in leakage currents that manifest as a small slope in the voltammograms. This affects the pseudocapacitive charges but not the OER current, which is severely limited by mass transport restrictions within the gap. The Ir(100) samples were measured in a hanging meniscus cell[61] due to the different geometric shapes of these crystals (disc-shaped instead of hat-shaped). In this cell, the electrode is in contact with a free-standing electrolyte meniscus, which provides a better-defined geometric sample area, but limits the accessible potential range to that of low OER currents (≤2 mA cm$^{-2}$). In all experiments, the samples were mounted in air and brought in contact with the electrolyte under open-circuit conditions. Then, potential control was established with a potentiostat (Ivium CompactStat) using a Ag/AgCl reference electrode (3.4 M) connected via a glass capillary and either a glassy carbon rod or a Pt wire installed in the outflow as a counter electrode. For comparison with the literature, all potentials in this work are referred with respect to the reversible hydrogen electrode (RHE).

All measurements were performed in 0.1 M NaOH (pH = 13), made from NaOH (Sigma-Aldrich, suprapure) and Milli-Q water. The electrolyte was continuously exchanged at a rate of 5 $\mu$L/s, using a remote-controlled pump system. This prevents the accumulation of radicals generated by the X-ray beam.

## 3. RESULTS

**3.1. Structure and Morphology of the $Co_3O_4$ Films.** Prior to studies in an electrochemical environment, the prepared thin films were characterized *ex situ* using SXRD and AFM. Figure 1a, which shows crystal truncation rods (CTRs) of the samples at an in-plane scattering vector $q_{inplane}$ = 2.5385 Å$^{-1}$, demonstrates that all deposited films consist of spinel-type cobalt oxide, i.e., $Co_3O_4$, with the (111) orientation. On all surfaces, including those with a square symmetry (Au(100) and Ir(100)), only the (111) orientation


https://doi.org/10.1021/acscatal.1c05169
ACS Catal. 2022, 12, 3256−3268

Table 1. Overview of the $Co_3O_4$ Samples Presented in this Study and Their Respective Deposition Conditions[a]

| sample | substrate | method | $d_\perp$ (nm) | $d_\parallel$ (nm) | $d_{island}$ (nm) | $\sigma$ |
|---|---|---|---|---|---|---|
| $Co_3O_4$/Ir(100) | Ir(100) | PVD in UHV | 15 | 18 | 22 | 1.07 |
| $Co_3O_4$/CoOOH-1M | CoOOH(001)/Au(111) | ED in 1 M NaOH | 15 | 19 | 62 | 1.08 |
| $Co_3O_4$/Au(111)-1M | Au(111) | | 18 | 18 | 52 | 1.04 |
| $Co_3O_4$/Au(100)-2M | Au(100) | ED in 2 M NaOH | 12 | 14 | 54 | 1.5 |
| $Co_3O_4$/Au(111)-2M | Au(111) | | 24 | 35 | 31 | 1.15 |

[a]The average film thickness $d_\perp$ and in-plane grain size $d_\parallel$ were obtained by XRD, whereas the lateral island size $d_{island}$ and the roughness factor $\sigma$ were obtained from the AFM measurements.

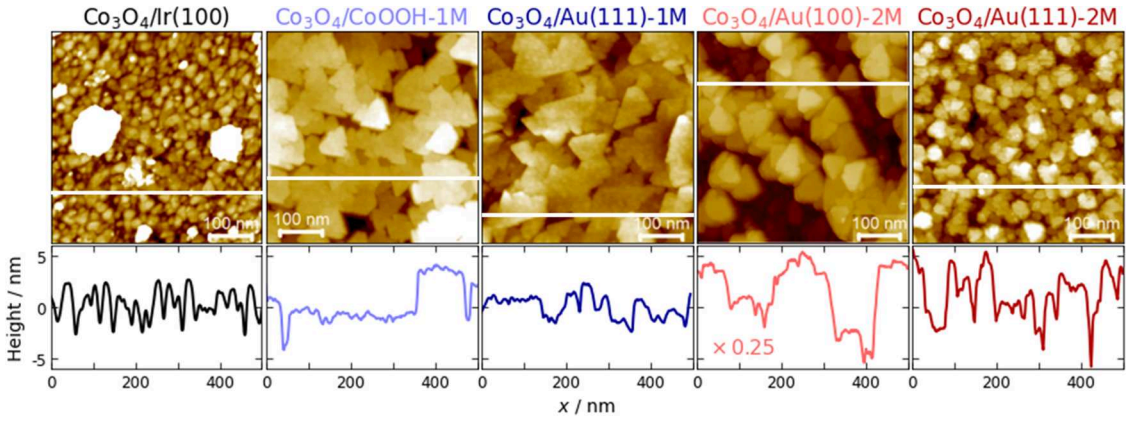


**Figure 2.** AFM images of the five samples obtained before immersion in the electrolyte. The bottom row shows horizontal cross-sections through the image (marked by white lines in the images).

is observed. This is in agreement with previous work on electrodeposited or PVD-grown $Co_3O_4$ films.[5−10] In addition, all deposits have a well-defined epitaxial arrangement with respect to the substrate lattice. In the accessible $q$-range $0 < q_z < 5$ Å$^{-1}$, six bulk diffraction peaks for $Co_3O_4$ are observed (marked by solid lines), which can be identified as the $(\bar{1}\bar{1}3)$, $(2\bar{2}2)$, (004), (115), (404), and (226) peaks of a (111)-oriented $Co_3O_4$ film. These ($HKL$) indices are given with respect to the simple cubic $Co_3O_4$ unit cell to facilitate comparison with the literature.

Table 1 gives an overview of selected samples, their respective deposition conditions, and the resulting film properties. In the following, samples will be denoted as "$Co_3O_4$/substrate-1M or -2M" to indicate on which substrate the $Co_3O_4$ film is deposited and, for the films on Au(111), whether the films were prepared in 1 M or 2 M NaOH. For the sake of clarity, only *operando* SXRD and electrochemical characterization of the samples listed in Table 1 are shown in the main text. However, three further samples, obtained by the same preparation methods, were also characterized by *operando* SXRD. Corresponding data, given in the supplementary information (Table S1), will be used in the global discussion.

Because the Ir(100) and Au(100) surfaces have a square and the Au(111) and CoOOH(001) surfaces have hexagonal symmetry, different in-plane arrangements are expected for the $Co_3O_4$(111) deposits. We observe that for $Co_3O_4$/Ir(100) and $Co_3O_4$/Au(100)-2M, the $Co_3O_4$ $[1\bar{1}2]$ direction is oriented along the [100] and [010] directions of the substrate lattice (Figure 1b). The latter is in agreement with previous results.[6,8−10,59] The resulting lattice mismatch is quite large, 17% for $Co_3O_4$/Au(100)-2M and 10% for $Co_3O_4$/Ir(100). In contrast, for the $Co_3O_4$ films on Au(111) and CoOOH(001)/Au(111), both the film and the substrate have a hexagonal in-plane arrangement where the $[1\bar{1}2]$ directions of the $Co_3O_4$ deposit and the Au(111) lattice are aligned. Here, the lattice mismatch is only 0.9%.

For $Co_3O_4$/CoOOH-1M, the CTR shows three additional peaks (Figure 1a, dashed lines), which are identified as the (012), (017), and (018) peaks of the underlying CoOOH(001) film. They appear on the CTR because they are located at almost exactly the same in-plane position. These CoOOH peaks are also weakly present on the CTR of $Co_3O_4$/Au(100)-2M, revealing that this sample is not completely pure-phase $Co_3O_4$ and contains a minor CoOOH component.

Atomic force microscopy (Figure 2) observations indicate that all deposits exhibit a granular morphology, are highly homogeneous, and cover the substrate completely. In the case of the Au(100) substrate, the darker areas of the AFM image are also covered by $Co_3O_4$ islands with smaller heights. The islands typically have a smooth top, terminated by a $Co_3O_4$(111) surface, and a triangular or hexagonal shape, with edges that are oriented at angles of 120° with respect to each other and which are parallel to the main lattice directions of the underlying single crystalline substrate. This morphology is in accordance with the epitaxial nature of the $Co_3O_4$ films and suggests that the films are fully crystalline.

The main difference between the different types of deposits is the in-plane island size and the surface roughness, which depend on the preparation conditions. In accordance with the literature,[8,9,59,60] the PVD-prepared $Co_3O_4$/Ir(100) samples are composed of a high density of (111) oriented tightly packed islands of similar height. $Co_3O_4$ electrodeposition in 1 M NaOH ($Co_3O_4$/Au(111)-1M and $Co_3O_4$/CoOOH-1M) results in films that consist of large, tightly packed islands with extended (111) top surfaces. Films with more disconnected three-dimensional islands are deposited from electrolytes containing 2 M NaOH ($Co_3O_4$/Au(111)-2M and $Co_3O_4$/


https://doi.org/10.1021/acscatal.1c05169
ACS Catal. 2022, 12, 3256−3268

Au(100)-2M). In this case, the side walls of the islands constitute a considerable fraction of the total oxide surface that is exposed to the electrolyte. For $Co_3O_4$/Au(111)-2M, these side walls are in addition oriented only loosely along well-defined lattice directions and, therefore, will be composed at least partly of surface orientations that differ from $Co_3O_4$(111).

A more quantitative analysis of the morphology was performed by determining the average in-plane size of $Co_3O_4$ islands in the AFM images ($d_{island}$) as well as the in-plane grain size ($d_{||}$), obtained from the in-plane width of $Co_3O_4$ Bragg reflections in the SXRD data (see Table 1). Notably, $d_{island}$ considerably exceeds $d_{||}$ in many of the samples. In particular, this is found in $Co_3O_4$/Au(111)-1M and $Co_3O_4$/CoOOH-1M films, which consist of triangular islands with long straight edges that reflect the epitaxial growth and (111) orientation of the $Co_3O_4$ film. Here, $d_{island}$ is ≈3 times larger than $d_{||}$ (Table 1), indicating that despite their flat-top surface, the islands consist of several grains separated by narrow grain boundaries, which may not be resolvable by AFM. Previous UHV-STM studies of $Co_3O_4$/Ir(100) films grown by PVD[59] suggest the presence of such narrow grain boundaries within the oxide film islands.

If we assume that the grain boundaries are too narrow for major electrolyte penetration, only a fraction of the vertical edges of the grains is in full contact with the bulk electrolyte in $Co_3O_4$ films electrodeposited in 1 M NaOH. In contrast, for electrodeposits formed in 2M NaOH, where $d_{island} \approx d_{||}$, the oxide film consists of free-standing three-dimensional islands consisting of typically just one grain. Thus, all of the edges of each grain are exposed to the electrolyte. This morphological difference will have to be kept in mind to understand the difference in the potential-dependent changes of these samples.

The electrochemically active surface area (ECSA) of the films is determined from the roughness factor $\sigma$ obtained from the AFM images (Table 1). For the films deposited in 1 M NaOH and the PVD films, $\sigma$ is close to 1. The highest $\sigma$ value is found for $Co_3O_4$/Au(100)-2M, followed by $Co_3O_4$/Au(111)-2M. For the latter, the true roughness most likely is somewhat underestimated by $\sigma$ because of the small size of the three-dimensional (3D) oxide islands and resulting convolution effects with the finite AFM tip size. A conservative estimation yields an upper limit of 3.2−4.5 for the $Co_3O_4$/Au(111)-2M samples (see Supporting Information, Section S4). Still, this is much smaller than the differences in electrocatalytic activity discussed in the following. Thus, simple geometric effects can be ruled out for explaining the different properties of the samples.

**3.2. Electrochemical Behavior.** The catalytic properties of the different samples were characterized in a solution of 0.1 M NaOH, where the $Co_3O_4$ films are very stable. The samples were found to withstand many potential cycles into the OER regime, performed over several hours, without irreversible structural changes or changes in the cyclic voltammograms (CVs) as long as the potential was kept positive of 0.77 V (see Supporting Information, Figures S2 and S3). This also indicates the absence of significant Fe impurities under the employed experimental conditions, which are known to result in progressive shifts in the CVs with time.[62] The CVs presented in Figure 3 were acquired in the SXRD cells described above and are corrected for the IR drop in solution.

The OER overpotential $\eta$, determined for a current density of $j$ = 1 mA cm$^{-2}$, differs for the different families of samples (Tables 2 and S1), with $Co_3O_4$/Ir(100) showing the highest

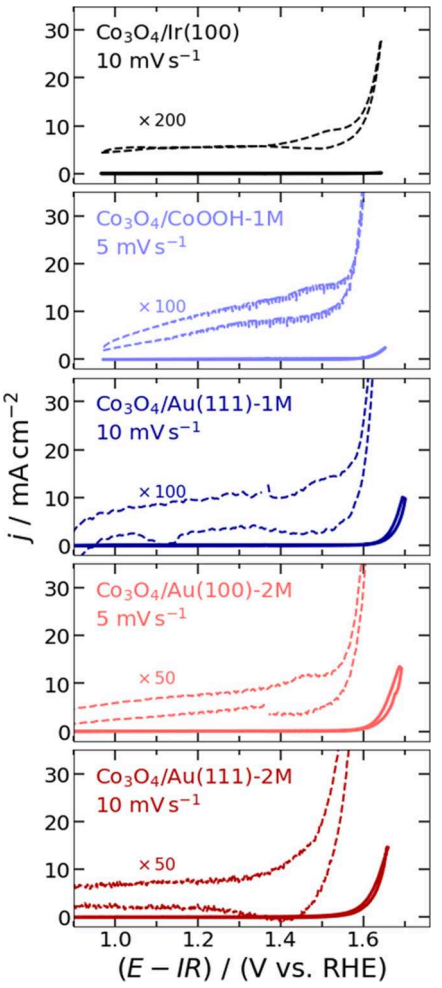


**Figure 3.** Cyclic voltammograms of the five samples in 0.1 M NaOH (pH = 13). Dashed lines show the pre-OER region with $j$ multiplied by a scaling factor and offset by 5 mA cm$^{-2}$ for clarity. All potentials are IR-corrected; current densities are corrected by roughness factor $\sigma$ of the oxide film.

value of $\eta$, i.e., the lowest activity. The oxides electrodeposited from 1 M NaOH ($Co_3O_4$/Au(111)-1M and $Co_3O_4$/CoOOH-1M) have intermediate OER activity, and those deposited from 2 M NaOH ($Co_3O_4$/Au(111)-2M and $Co_3O_4$/Au(100)-2M) are the most active catalysts. Overall, the overpotentials vary by up to 120 mV, corresponding to 2 orders of magnitude difference in the OER current densities at a fixed potential (Table S1). The Tafel slopes (Tables 2 and S1) are similar for all samples, suggesting a similar rate-determining step of the OER. They are comparable to those found in previous studies of the OER on Co oxide catalysts at pH 13.[63]

In the pre-OER regime, the CVs of the four samples (Figure 3) prepared by electrodeposition exhibit a comparable shape, which is in accordance with CVs reported in the literature.[2,12] The current in the range of 30 to 100 $\mu$A cm$^{-2}$ is much larger than what would be expected for simple double-layer charging and is attributed to pseudocapacitive processes.[7,16,45] Near the onset of the OER, a pair of redox waves is found at about 1.45 V, which is close to the CoOOH/$CoO_2$ equilibrium potential.[2,12,64] In the CV of the PVD-deposited sample, $Co_3O_4$/Ir(100), similar albeit much weaker redox peaks are found, and the pseudocapacitive current is only a few $\mu$A cm$^{-2}$ in the potential range below 1.4 V. The low current density of


https://doi.org/10.1021/acscatal.1c05169
ACS Catal. 2022, 12, 3256−3268

Table 2. Electrocatalytic and Structural Data of $Co_3O_4$ Samples Presented in This Study[a]

| sample | Tafel slope (mV dec$^{-1}$) | $\eta$ (V) | $\Delta d_\perp$ (nm) | $\Delta d_\parallel$ (nm) | $\Delta\varepsilon_\perp$ (%) | $\Delta\varepsilon_\parallel$ (%) |
|---|---|---|---|---|---|---|
| $Co_3O_4$/Ir(100) | 67 | 0.474 | 0 | 0.1 | 0.01 | 0.01 |
| $Co_3O_4$/CoOOH-1M | 56 | 0.411 | 0.3 | 0.2 | 0.15 | 0.01 |
| $Co_3O_4$/Au(111)-1M | 57 | 0.422 | 0.2 | 0.1 | 0.17 | 0.05 |
| $Co_3O_4$/Au(100)-2M | 64 | 0.396 | 0.3 | 0.9 | 0.43 | 0.24 |
| $Co_3O_4$/Au(111)-2M | 67 | 0.351 | 0.7 | 2.2 | 0.53 | 0.19 |

[a]Given are the Tafel slope and the OER overpotential $\eta$ for a current density of 1 mA cm$^{-2}$, the changes in in-plane ($\Delta d_\parallel$) and out-of-plane ($\Delta d_\perp$) grain size between 1.00 and 1.65 V, and the relative changes in-plane ($\Delta\varepsilon_\parallel$) and out-of-plane ($\Delta\varepsilon_\perp$) strain over this potential range.

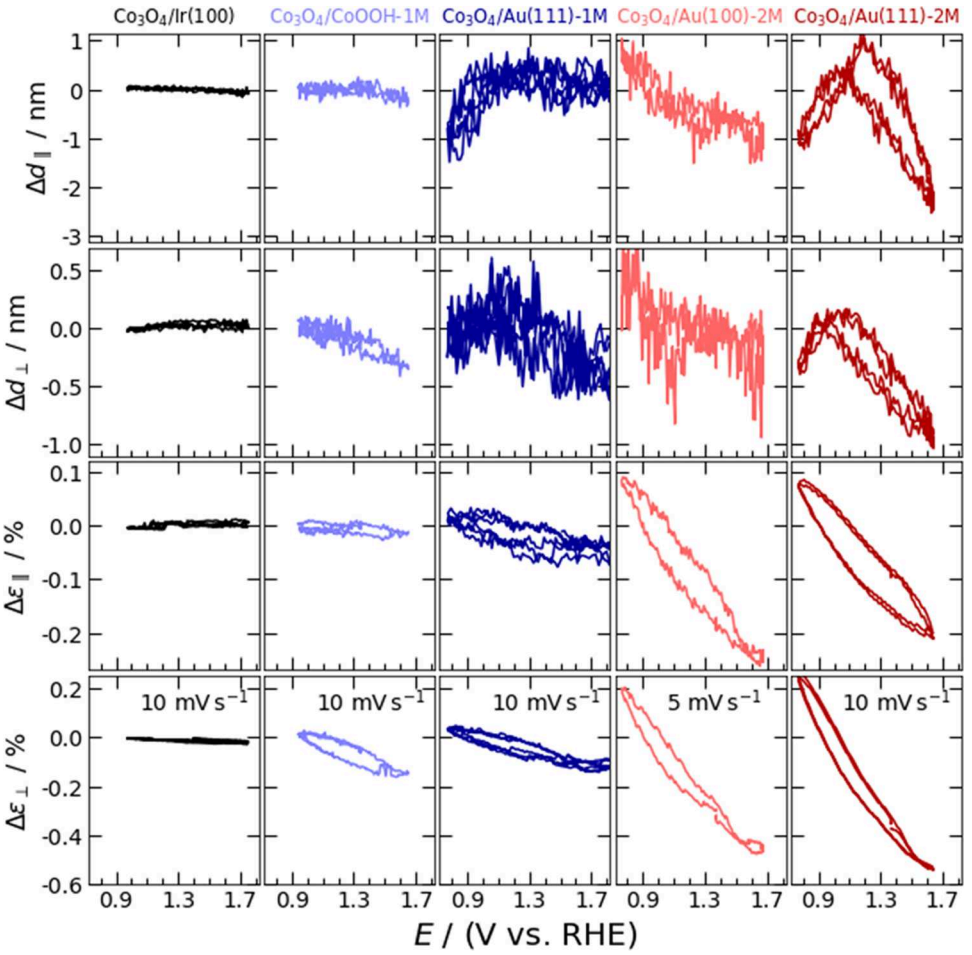


**Figure 4.** *Operando* surface X-ray diffraction of the five samples performed during cyclic voltammetry in 0.1 M NaOH, showing from top to bottom the change in in-plane grain size, the change in out-of-plane grain size, the change in in-plane strain, and the change in out-of-plane strain. Potentials were IR-corrected. As a reference point for the strain and grain size changes, $E$ = 1.00 V was chosen.

the latter sample is in accordance with previous electrochemical measurements.[9]

**3.3. *Operando* SXRD Measurements.** Structural changes in the film were monitored by *operando* surface X-ray diffraction measurements. The same method as in our previous studies of Co oxide catalysts was employed.[7] Together with the electrochemical current, four structural parameters were obtained simultaneously from two-dimensional (2D) detector images of a $Co_3O_4$ Bragg peak as a function of potential. The in-plane ($d_\parallel$) and out-of-plane ($d_\perp$) grain size, which was obtained from the horizontal and vertical full width at half maximum (FWHM) of the Bragg peak via $d = 2\pi/\sigma_{FWHM}$, and the in-plane ($\varepsilon_\parallel$) and out-of-plane ($\varepsilon_\perp$) strain, calculated from the positional shift of the Bragg peak's in-plane and out-of-plane scattering vector via $\varepsilon = q_{bulk}/q - 1$ (see Supporting Information, Section S1 and Figure S5 for characteristic raw data). Measurements were performed at two different peaks, namely, *HKL* = (404) and (131), which gave comparable results. To ease the comparison between the different samples, the changes in grain size and relative strain changes are plotted using 1 V as the reference state of the sample. The SXRD data obtained in an inert gas atmosphere prior to immersion and after immersion at 1 V provide an almost identical height $d_\perp$ of the grains, i.e., of the film thickness. This indicates that no major electrolyte-induced restructuring of the $Co_3O_4$(111) surface occurs at this potential, making it a suitable reference point.

*Operando* SXRD results on the structural changes during the potential cycles in 0.1 M NaOH are summarized in Figure 4 and Table 2. The PVD-prepared sample ($Co_3O_4$/Ir(100))


https://doi.org/10.1021/acscatal.1c05169
ACS Catal. 2022, 12, 3256−3268

stays unchanged in the full potential range. There are no changes in grain size and strain within the experimental detection limits (<0.01% in $\Delta\varepsilon$; <0.1 nm in $\Delta d$). In contrast, all electrodeposited samples exhibit reversible grain size and strain changes as a function of potential, which are highly reproducible in successive cycles (see data for $Co_3O_4$/Au(111)-1M and $Co_3O_4$/Au(111)-2M for examples). As discussed previously,[7] the hysteresis between the positive and negative potential sweep is attributed to the finite potential sweep rate. In potential step experiments (Figure S7), the skin formation occurred on timescales of a couple of seconds and the resulting steady-state changes in grain size were similar as in the potential sweep measurements. This is in accordance with our previous work, where similar structural changes were found in SXRD measurements performed at scan rates of 10 and 50 mV/s and under stationary conditions.[7]

The amplitude of the structural changes differs substantially for the differently prepared $Co_3O_4$(111) films. In general, the largest changes are found for the samples prepared in the 2 M NaOH electrolyte ($Co_3O_4$/Au(100)-2M and, in particular, $Co_3O_4$/Au(111)-2M) and the smallest for $Co_3O_4$/Ir(100). We mention in passing that for $Co_3O_4$/Au(111)-1M and $Co_3O_4$/Au(111)-2M, a decrease in grain size is also observed at potentials <1 V. It can be attributed to the initial stage of $Co_3O_4$ conversion to $Co(OH)_2$ and will not be discussed here further.[7]

For a more detailed analysis, we first discuss the horizontal and vertical strain (Figure 4, bottom two rows). For all electrodeposited samples, both $\Delta\varepsilon_{\parallel}$ and $\Delta\varepsilon_{\perp}$ are negative and increase in magnitude with the increasing potential, indicating a lattice contraction, i.e., a shrinking of the $Co_3O_4$ unit cell volume. Moreover, the magnitude of the $\Delta\varepsilon_{\perp}$ change is roughly twice that of $\Delta\varepsilon_{\parallel}$. The larger $\Delta\varepsilon_{\perp}$ value may be expected, as the in-plane expansion and contraction of the $Co_3O_4$ islands are constricted by epitaxial clamping to the substrate lattice and neighboring islands. The variations of $\Delta\varepsilon_{\parallel}$ and $\Delta\varepsilon_{\perp}$ are rather monotonous over the entire pre-OER range, but in some cases seem to become less pronounced near the onset of the OER (especially for $\Delta\varepsilon_{\perp}$). For the samples grown in 2 M NaOH ($Co_3O_4$/Au(100)-2M and $Co_3O_4$/Au(111)-2M), the potential dependence is 4−10 times larger than for samples grown in 1 M NaOH ($Co_3O_4$/Au(111)-1M and $Co_3O_4$/CoOOH-1M).

A more complex behavior is found for the horizontal and vertical change in average grain size ($\Delta d_{\parallel}$ and $\Delta d_{\perp}$) (Figure 4, top two rows). As mentioned in the introduction, these changes are related to the reversible structural transformation of the oxide surface region at potentials >1.15 V, resulting in the formation of a skin layer (Figure 5a). In agreement with the previous studies of this phenomenon, we observe no diffraction peaks of other Co oxide or oxyhydroxide phases in this potential regime and thus likewise attribute the skin layer to an X-ray amorphous $CoO_x(OH)_y$ phase with an increased Co oxidation state.[2,3,7] This increase in oxidation state was also confirmed for the electrodeposited $Co_3O_4$(111) films in preliminary *in situ* XAS experiments (to be published). The X-ray amorphous nature of the skin layer implies that the sublattice of the Co ions, which dominates the X-ray diffraction, has to be disordered. This is in full agreement with assumptions based on the coordination of the cations in the spinel lattice, where $Co^{2+}$ occupy the tetrahedral (Th) sites and $Co^{3+}$ the octahedral (Oh) sites, respectively. Oxidation of the $Co^{2+}$ will thus require a change in their coordination,

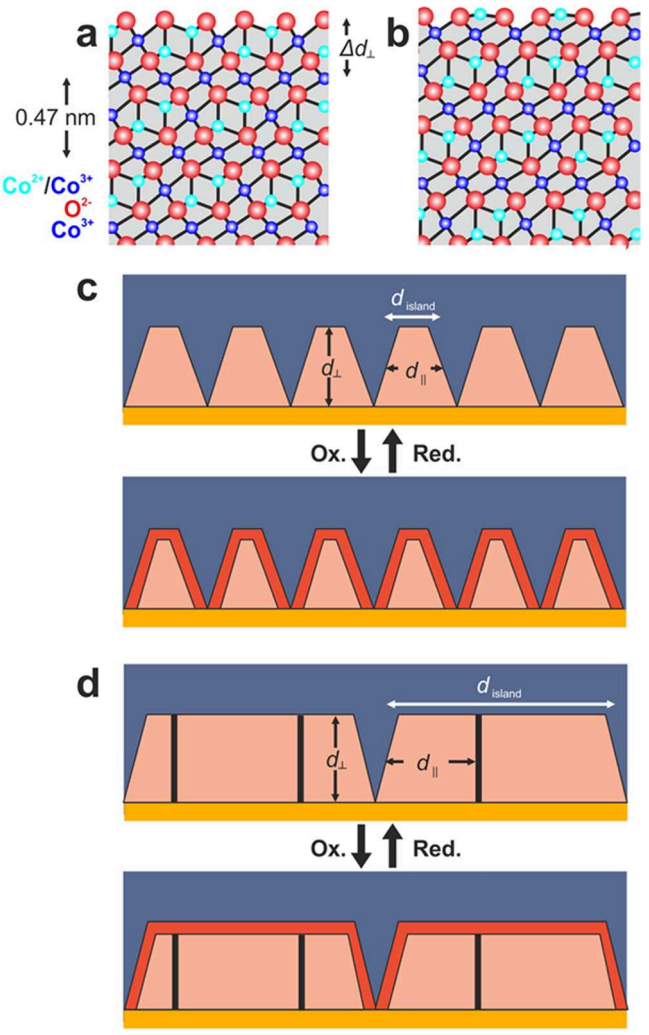


**Figure 5.** Schematic models of the crystal structure of (a) electrodeposited $Co_3O_4$(111) films prior to skin layer formation and (b) PVD-prepared $Co_3O_4$(111) films. (c,d) Scheme of the $Co_3O_4$ film morphology formed by deposition in (c) 2 M NaOH and (d) 1 M NaOH, illustrating the structure at potentials <1.15 V (top) and after the formation of the skin layer (indicated in red) at more oxidative potentials in the OER range (bottom). Grain boundaries in the islands are depicted by black lines.

resulting in the disordering of the metal sublattice. On the basis of X-ray absorption spectroscopy results, Bergmann et al. proposed that the Co oxidation state increases within the pseudocubic close-packed $O^{2-}$ lattice under retention of the Co coordination but that at more positive potentials amorphization occurs, accompanied by a partial change in Co coordination from tetrahedral to octahedral and a slight rearrangement of the $O^{2-}$ lattice.[2,3] This rather local structural rearrangement would facilitate the reversible transformation of the $Co_3O_4$ in the skin layer region.

The skin layer starts to form at potentials of roughly 1.15 V, which is several hundred mV negative of the OER regime. As already discussed in our previous work,[7] this onset potential is in good agreement with the thermodynamic equilibrium potential for the transition between $Co_3O_4$ and CoOOH[64]

$$Co_3O_4 + OH^- + H_2O \leftrightarrow 3CoOOH + e^- \quad (E_{eq} = 1.22\ V_{RHE})$$



https://doi.org/10.1021/acscatal.1c05169
ACS Catal. 2022, 12, 3256−3268

Thus, the reversible skin layer formation has to be attributed to the oxide redox chemistry rather than the OER. The charge transfer associated with this reaction contributes to the pseudocapacitive current in the pre-OER regime.

The amount of skin layer formation differs for the different samples. Between 1.15 and 1.55 V, $\Delta d_{\parallel}$ and $\Delta d_{\perp}$ are largest for $Co_3O_4$/Au(111)-2M. For the other electrodeposited samples, the $\Delta d_{\perp}$ changes have similar values. The situation is different for $\Delta d_{\parallel}$, where the decrease is still ≈1 nm for $Co_3O_4$/Au(100)-2M but <0.2 nm for $Co_3O_4$/Au(111)-1M and $Co_3O_4$/CoOOH-1M. This difference can be partly explained by a geometric effect. In the case of $Co_3O_4$/Au(100)-2M and $Co_3O_4$/Au(111)-2M, in which a large fraction of the grains' side walls is exposed to the electrolyte, significant changes in horizontal and vertical grain size are observed, with $\Delta d_{\parallel} > \Delta d_{\perp}$. These indicate that the skin layer forms everywhere on the top and sides of the oxide grain, as already proposed in our previous study (Figure 5c).[7] For flat-top films electrodeposited in 1 M NaOH (Figure 5d), the vertical changes $\Delta d_{\perp}$ are only 0.3 ± 0.1 nm, which suggests that on planar $Co_3O_4(111)$ surfaces, only a single Co layer is transformed during skin layer formation. Here, the $\Delta d_{\parallel}$ changes are much smaller. Taking into account that $d_{\parallel} \approx d_{island}/3$, the islands in these islands have to contain internal domain boundaries, which are narrow (see above). It is likely that the skin layer forms at the islands' external facets only and not at the internal grain boundaries, resulting in an effective reduction of $\Delta d_{\parallel}$ (Figure 5d). However, as we show below, the differences in the amount of formed skin layer are substantially larger than those that can be accounted for by the differences in the sample morphology.

In contrast to the electrodeposited oxides, the PVD-deposited $Co_3O_4$/Ir(100) samples remain structurally unchanged. For these films, the potential-dependent changes in grain size and strain are negligible, with $\Delta d_{\parallel}$ and $\Delta d_{\perp}$ being both <1 Å and $\Delta\varepsilon_{\parallel}$ and $\Delta\varepsilon_{\perp}$ being less than 0.03%. These observations indicate that no skin layer forms on these samples, especially also not on the islands' top surfaces. This is surprising, taking into account the identical crystal structure and (111) surface orientation of the oxide film as compared to the electrodeposited films. This behavior differs from that of all electrodeposited films, where even on extended flat $Co_3O_4(111)$ islands, a thin skin layer forms.

The structural stability of PVD-deposited $Co_3O_4$/Ir(100) has to be attributed to the different preparation method, which is a high-temperature process in a water-free environment. Previously detailed STM/LEED-IV studies of PVD-prepared oxide layers in UHV revealed that the top of the islands is atomically smooth and exhibits a characteristic surface structure.[59] Specifically, the $Co_3O_4(111)$ surface is terminated by a sublayer of $Co^{2+}$ cations (half-filled) residing on an $O^{2-}$ layer, followed by a $Co^{3+}$ cation layer (Figure 5b). The layer spacing between the top $Co^{2+}$ and subsequent $O^{2-}$ layer is strongly contracted as compared to the $Co_3O_4$ bulk spinel lattice, and the $O^{2-}$ ions in the surface layer exhibit almost no vertical buckling but slight in-plane relaxations. It was shown that this structure survives the transfer to the alkaline electrolyte,[9] although slight changes in the terminal atoms may occur, e.g., due to surface hydroxylation. Therefore, oxidation of the topmost $Co^{2+}$ cations in the pre-OER regime is expected above 1.15 V, which leads to a surface region that contains two planes of $Co^{3+}$ cations at the onset potential of the OER. This likely suppresses further surface restructuring in the vertical direction, taking into account that also for planar $Co_3O_4(111)$ surfaces of electrodeposited films, only the 2 topmost Co atomic layers are transformed ($\Delta d_{\parallel}$ < 0.5 nm). From a structural viewpoint, oxidation of the topmost $Co^{2+}$ cation plane, which already deviates from the bulk lattice structure, should not be detectable by SXRD, even if this would lead to a relaxation of its atomic positions. Further support for this scenario comes from recent SXRD observations for UHV-prepared $Fe_3O_4(100)$ single crystals in NaOH solution.[65] For this oxide, the presence of a reconstructed surface layer, which extends over three cationic planes and exclusively contains $Fe^{3+}$ ions, was found to be sufficient to stabilize the structure of $Fe_3O_4$ bulk and no skin was observed including in the OER regime.[65]

## 4. DISCUSSION

**4.1. Reversible Potential-Induced Structural Changes.** Our study reveals two major differences in the potential-dependent structure of the electrodeposited samples with respect to those prepared by PVD. For the electrodeposited samples, we observe the formation of a skin layer (indicated by a decrease of $d_{\perp}$ and $d_{\parallel}$). Second, we find a simultaneous shrinkage of the $Co_3O_4$ bulk lattice, i.e., a reversible decrease of the unit cell volume $\Delta V/V = \Delta\varepsilon_{\perp} + 2\Delta\varepsilon_{\parallel}$ ($\Delta\varepsilon_{\perp}$ and $\Delta\varepsilon_{\parallel}$ are <0) (see Table S1). These two effects are strongly correlated; samples with thicker skin layers also exhibit larger bulk lattice changes. In the case of the PVD-prepared samples, no skin layer is formed, $\Delta V/V$ does not change significantly, and the sample structure remains unchanged over the entire studied potential range (see Figure 4).

The potential-induced strain in the horizontal and vertical direction, $\Delta\varepsilon_{\parallel}$ and $\Delta\varepsilon_{\perp}$, is strongly correlated with the thickness of the formed skin layer (Figure 6). This suggests

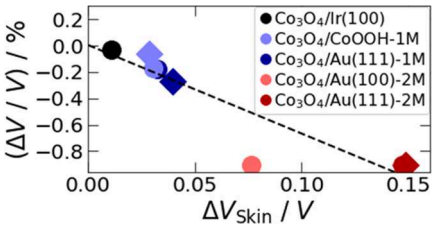


**Figure 6.** Plot of the relative volume change $\Delta V/V$ as a function of the skin volume fraction $V_{skin}/V$. Circles correspond to the samples shown in Figures 1−4 and diamonds correspond to auxiliary measurements.

that the strain is at least partly induced by the skin layer formation. Because of the increase in the Co oxidation state in the $CoO_x(OH)_y$ phase, a decrease in the Co−O bond length is expected, corresponding to a compressive strain. This strain is transmitted to the $Co_3O_4$ bulk lattice. Because the oxide grain sizes are much smaller than the typical decay length for lattice strain, which is in the $\mu$m range within oxide single crystals,[66] the strain should be rather uniformly distributed across the oxide grain. Within this scenario, we expect that $\Delta\varepsilon_{\parallel}$ and $\Delta\varepsilon_{\perp}$ and thus also $\Delta V/V$ should decrease approximately proportionally to the volume fraction of the grain that is converted into the $CoO_x(OH)_y$ skin layer, $V_{skin}/V$ (see Supporting Information, Section S2 for the determination of $V_{skin}/V$). This is indeed observed in the SXRD data (Figure 6). A closer look at these data further shows that the amplitude of $\Delta V/V$ is a function of the oxide morphology. It is largest for oxides grown


https://doi.org/10.1021/acscatal.1c05169
ACS Catal. 2022, 12, 3256−3268

in 2 M NaOH, where the islands consist of single grains, which expose all of their lateral facets to the electrolyte. The magnitude of the overall strain changes that would be expected due to the oxidation state change in the skin layer can be estimated to be in the range of $5 \times 10^{-4}$ to $5 \times 10^{-3}$ for the studied samples (see Supporting Information, Section S3), which is in good agreement with the SXRD experiments.

In a similar way, the strain changes negative of 1 V may be explained by the gradual transformation of $Co_3O_4$ into $Co(OH)_2$, i.e., a material with an even lower mean Co oxidation state. The observed direction of the strain changes over the full potential range is in full accordance with this scenario.

**4.2. Impact of the Skin Layer on OER Activity.** For the electrodeposited films, the $Co_3O_4$ is covered in the OER regime by the skin layer (Figure 5a), which does not result from the OER but from the oxide chemistry[7] and which is the OER-active phase. Figure 7 shows that the OER activity of the

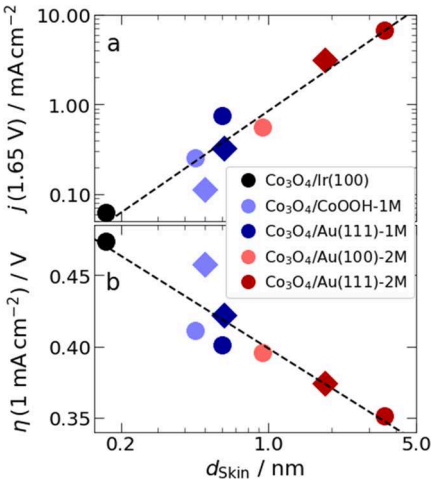


**Figure 7.** Plots of (a) the current density at an overpotential of 420 mV and (b) the overpotential $\eta$ necessary to reach an OER current density of 1 mA $cm_{ECSA}^{-2}$ as a function of the average skin layer thickness $\langle d_{skin} \rangle$. Circles correspond to the samples shown in Figures 1−4 and diamonds correspond to auxiliary measurements.

$Co_3O_4$ films increases with the skin volume per electrode surface area. This quantity corresponds to a length that we denote in the following as $\langle d_{skin} \rangle$ (calculated as described in Section S2 of the Supporting Information). The true meaning of this length is discussed below. At a fixed potential of 1.65 V (Figure 7a), the current is clearly correlated with $\langle d_{skin} \rangle$. The current reaches 10 mA $cm^{-2}$ for the samples grown in 2 M NaOH, which exhibits the largest $\langle d_{skin} \rangle$, while it is about two-decade smaller for the $Co_3O_4$/Ir(100) film, onto which nearly no skin develops (see Table S1). Correspondingly, at a fixed current density of 1 mA $cm^{-2}$ (Figure 7b), the OER overpotential decreases with increasing $\langle d_{skin} \rangle$ from 360 mV for $Co_3O_4$/Au(111)-2M to 480 mV for $Co_3O_4$/Ir(100). As already discussed in Section 3.1, this difference cannot be caused solely by the differences in the microscopic roughness of the oxide films, which is at most a factor of 4.5. Thus, it has to be attributed to the actual differences in the average skin layer thickness of the studied samples. Most probably, these are related to the different surface terminations of the $Co_3O_4$ islands. Our observations indicate that the skin layer is the smallest on the (surface reconstructed) PVD-prepared $Co_3O_4$(111) film. For electrodeposited films, the skin layer involves about 2 Co layers for the $Co_3O_4$(111) surface of films grown in 1 M NaOH and can be thicker than 4 Co layers on the side walls of the 3D islands of $Co_3O_4$/Au(111)-2M films, where also significant amounts other facets than $Co_3O_4$(111) are exposed to the electrolyte. In addition, also differences in the surface defect densities may play a role.

The observed correlation between $\langle d_{skin} \rangle$ and the electrocatalytic activity provides strong evidence that not only the oxide surface but the entire skin layer contributes to the OER. In other words, the skin is a three-dimensional OER zone that involves Co centers located within the very first atomic planes of the oxide catalyst. This conclusion explains the results by Jiao and Frei, who found that the photocatalytic water splitting efficient on $Co_3O_4$ nanoparticles does not scale with the particle surface.[58] It is also consistent with the interpretation of *operando* mass spectroscopy experiments by the Baltruschat group, which showed that lattice oxygen is involved in the reaction but that only oxygen sites close enough to the surface are exchanged with O from the solution.[44]

For a deeper microscopic understanding of the correlation between $\langle d_{skin} \rangle$ and the OER activity, we again consider the atomic-scale structure of the $CoO_x(OH)_y$ skin layer phase at the oxide surface. As discussed above as well as in many previous studies, the change in the oxidation state will lead to a Co coordination change and pronounced lattice disordering. This should result in defects such as pores and nanoscale surface roughness, which will make sites below the surface accessible and thus increase the effective density of active reaction sites. We propose that these defects are of subnanometer dimensions and form by highly local restructuring. This is supported by the very high reversibility of the structural changes. Even many skin formation/recrystallization cycles do not lead to changes in the film morphology or quantitative grain sizes, indicating that long-range restructuring is unlikely (see AFM images in Figure S2). In addition, the presence of defects will increase oxygen mobility within the skin layer. This will enhance reaction pathways that involve lattice oxygen, which can be more easily supplied than in the spinel structure.

Our SXRD data provide the average thickness $\langle d_{skin} \rangle$ of $Co_3O_4$ that is converted into the skin layer. In the literature, the TOF is calculated very often with respect to the total number of Co centers within the entire sample. Here, we estimate the TOF by assuming that all of the Co centers within the skin are contributing equally to the OER. Using the known Co ion density in $Co_3O_4$ (24 per $(8.0837\ Å)^3$ unit cell), we can estimate the number of sites involved in the OER as $\langle n_{skin} \rangle = 4.54 \times 10^{15}\ cm^{-2} \times \langle d_{skin} \rangle$/nm. The OER turn-over frequency (TOF) of our $Co_3O_4$(111) films is therefore $TOF = j_{OER}/(4 \times e_0 \times \langle n_{skin} \rangle)$, This approach yields a TOF at 1.65 V that ranges between 0.12 $s^{-1}$ for $Co_3O_4$/Ir(100), the least active catalyst, and 0.64 $s^{-1}$ for $Co_3O_4$/Au(111)-2M, the most active catalyst. We will address this discrepancy further in the next section.

**4.3. How Many Sites does the OER Require?** The quantitative trends shown in Figure 7 provide additional mechanistic insight into the OER mechanism on $Co_3O_4$. The double logarithmic plot in Figure 7a gives a scaling relationship $j \propto \langle n_{skin} \rangle^{\kappa}$ with an exponent $\kappa \approx 1.6$ (dashed line) because $\langle n_{skin} \rangle$ is proportional to $\langle d_{skin} \rangle$. To understand the trends for the overpotential $\eta$ at a fixed value of $j_{OER}$ (Figure 7b), we consider the OER Tafel slope $b$ and write $j_{OER}(\eta) =$


https://doi.org/10.1021/acscatal.1c05169
ACS Catal. 2022, 12, 3256−3268

$e_0 z k_0 \langle n_{skin} \rangle^{\kappa} \times 10^{\eta/b}$, where $z$ is the charge transfer per evolved $O_2$ and $k_0$ is the rate constant. Using this expression, $\eta$ should decrease linearly with $\log\langle n_{skin} \rangle$, with the slope being $\kappa \cdot b$. Indeed, such a linear dependence is observed for the data shown in Figure 7b and the observed slope of −93 mV $dec^{-1}$ is in good agreement with the experimental value of the Tafel slope (≈60 mV $dec^{-1}$) times the exponent $\kappa \approx 1.6$. If we take this exponent into account in the calculation of the TOF, the factor of 5.3 between the values for $Co_3O_4$/Ir(100) and $Co_3O_4$/Au(111)-2M can be explained.

In principle, two explanations may account for the fact that the exponent $\kappa$ is clearly larger than one. First, the surface density of the OER sites may scale nonlinearly with that of the Co ions in the skin layer and, second, the OER may require more than one reaction site. The former seems less plausible, taking into account that quasi *in situ* EXAFS of $Co_3O_4$ did not evidence significant changes of the Co coordination shells between the pre-OER and OER conditions.[3] The second interpretation appears very likely, even though the OER is most commonly described as a four-step reaction mechanism involving a single site as assumed for the OER on Co oxide catalysts.[21] The question as to whether the OER requires one single or several sites has been debated for decades, in particular to account for the experimental value of the Tafel slope $b$.[67−69] More recent *operando* spectroscopic studies provide experimental evidence that the OER on Co oxides is a two-site reaction. Time-resolved IR studies of photocatalytic water oxidation on $Co_3O_4$ by Zhang et al. found a mechanism involving two neighboring lattice oxygen.[24] A similar mechanism was reported in *operando* X-ray absorption and Raman spectroscopy studies of CoOOH by Moysiadou et al., where the desorption of the adjacent oxygen atoms as $O_2$ was identified as the rate-determining step.[53] All of these observations are consistent with the high OER activity of molecular OER catalysts containing two Co centers (Co-OECs).[70] Furthermore, recent DFT studies of CoOOH likewise indicated that two-site OER mechanisms should be energetically preferred.[56,71]

For two-site mechanisms, the reaction rate should be proportional to $n_{skin}^2$ and an exponent $\kappa = 2$ would be expected. The lower value observed in our experiments could be rationalized by decreasing accessibility of the OER sites that are deeper within the skin layer. This seems reasonable, considering that for subsurface sites, mass transport within the $CoO_x(OH)_y$ phase is required.

## 5. CONCLUSIONS

Our results provide clear evidence that the disordered near-surface region forming reversibly on $Co_3O_4$ in the pre-OER regime, i.e., the X-ray amorphous skin layer, is a three-dimensional oxygen evolution reaction zone. This interphase region depends on the oxide surface orientation. For $Co_3O_4$(111) surfaces of electrodeposited samples, the transformation seems to be limited to the topmost two Co layers. Somewhat thicker interphase layers apparently form on other $Co_3O_4$ surface orientations, which are present on the side walls of the epitaxial oxide islands. For PVD-prepared $Co_3O_4$(111) films, the amount of reversibly formed skin layer is insignificant. The different amounts of the OER-reactive interphases explain why the OER activity of $Co_3O_4$(111) epitaxial films with the same bulk spinel structures may span over two decades, while the geometrical roughness of all samples spans a much narrower range. Using true *operando* SXRD, we measured the average thickness of the oxide that is converted into the skin layer and estimated the number of active sites within the skin layer on all samples. Moreover, the scaling law between the reaction rate and the site density indicates that two surface sites are involved in the OER.

These observations are relevant for the fundamental understanding of the oxide's reactivity as well as for developing strategies to activate the surface for the OER. Most studies implicitly assume that the catalytic reaction proceeds exclusively on the catalyst surface and involves adsorbates and surface lattice oxygen. If this would be the case, the transformation of the outmost atomic layer of the oxide into a phase with a higher oxidation state would be sufficient. The formation of thicker skin layers would not lead to increased activity and thus qualitative knowledge about the presence of a restructured surface would be sufficient for understanding the catalytic activity. Our results indicate that the OER activity directly scales with the thickness of the restructured skin layer over a range spanning several nanometers, i.e., length scales that strongly exceed those of an oxide monolayer. Fundamental understanding of the oxide's reactivity therefore requires quantitative data on the spatial extension of the restructured layer under OER conditions. Furthermore, the activity of such catalysts may be substantially boosted by activation strategies that promote the formation of thicker skin layers.

In fact, our results suggest that rather subtle differences in the surface morphology can have a large influence on the OER activity of $Co_3O_4$ catalysts. This may not only be the case for pure and doped $Co_3O_4$ but also for other spinel-type transition metal oxide catalysts. Thus, great care has to be taken in comparing the OER activity of differently prepared catalysts. The described surface morphology effects can make it difficult to derive a clear interpretation of the influence of catalyst preparation conditions or chemical modifications on its catalytic properties as long as the spatial extension of the reactive skin layer is not determined. On the other hand, these observations pave the way to a controlled surface engineering of such oxide catalysts. As illustrated in this work, the oxide morphology can be tuned by the deposition method. This allows preparation of highly stable oxide surfaces with a well-defined but low number of reaction sites, which are highly suitable for fundamental studies of the OER mechanism, as well as more reactive catalysts with surface orientations or chemical modifications that promote the formation of thicker OER-reactive interphase layers. These ideas, gained from model catalysts, may provide a basis for the targeted design of highly active real oxide catalysts.

## ■ ASSOCIATED CONTENT

### Supporting Information

The Supporting Information is available free of charge at https://pubs.acs.org/doi/10.1021/acscatal.1c05169.

Description of *operando* surface X-ray diffraction studies (scattering geometry, AFM images before and after potential cycling, cyclic voltammograms, Tafel plots, two-dimensional detector images, electrocatalytic and structural data of all investigated $Co_3O_4$ samples) (Section S1); estimation of skin volume and skin volume fraction (Section S2); estimation of the effect of oxidation state change on strain (Section S3); and



https://doi.org/10.1021/acscatal.1c05169
ACS Catal. 2022, 12, 3256−3268

estimation of the electrochemical surface area (Section S4) (PDF)

## AUTHOR INFORMATION


### Corresponding Authors

**Olaf M. Magnussen** − *Institute of Experimental and Applied Physics, Kiel University, 24118 Kiel, Germany;* orcid.org/0000-0003-4900-0880; Email: magnussen@physik.uni-kiel.de

**Fouad Maroun** − *Laboratoire de Physique de la Matière Condensée (PMC), CNRS, Ecole Polytechnique, Institut Polytechnique de Paris, 91120 Palaiseau, France;* Email: fouad.maroun@polytechnique.edu

**Philippe Allongue** − *Laboratoire de Physique de la Matière Condensée (PMC), CNRS, Ecole Polytechnique, Institut Polytechnique de Paris, 91120 Palaiseau, France;* orcid.org/0000-0001-9457-5312; Email: philippe.allongue@polytechnique.edu

### Authors

**Tim Wiegmann** − *Institute of Experimental and Applied Physics, Kiel University, 24118 Kiel, Germany;* orcid.org/0000-0001-8526-0474

**Ivan Pacheco** − *Laboratoire de Physique de la Matière Condensée (PMC), CNRS, Ecole Polytechnique, Institut Polytechnique de Paris, 91120 Palaiseau, France*

**Finn Reikowski** − *Institute of Experimental and Applied Physics, Kiel University, 24118 Kiel, Germany*

**Jochim Stettner** − *Institute of Experimental and Applied Physics, Kiel University, 24118 Kiel, Germany*

**Canrong Qiu** − *Institute of Experimental and Applied Physics, Kiel University, 24118 Kiel, Germany*

**Mathilde Bouvier** − *Laboratoire de Physique de la Matière Condensée (PMC), CNRS, Ecole Polytechnique, Institut Polytechnique de Paris, 91120 Palaiseau, France*

**Manon Bertram** − *Interface Research and Catalysis, Friedrich-Alexander-Universität Erlangen-Nürnberg, 91054 Erlangen, Germany*

**Firas Faisal** − *Interface Research and Catalysis, Friedrich-Alexander-Universität Erlangen-Nürnberg, 91054 Erlangen, Germany*

**Olaf Brummel** − *Interface Research and Catalysis, Friedrich-Alexander-Universität Erlangen-Nürnberg, 91054 Erlangen, Germany;* orcid.org/0000-0001-5968-0774

**Jörg Libuda** − *Interface Research and Catalysis, Friedrich-Alexander-Universität Erlangen-Nürnberg, 91054 Erlangen, Germany;* orcid.org/0000-0003-4713-5941

**Jakub Drnec** − *European Synchrotron Radiation Facility, 38000 Grenoble, France*

Complete contact information is available at: https://pubs.acs.org/10.1021/acscatal.1c05169


### Notes

The authors declare no competing financial interest.

## ACKNOWLEDGMENTS

The authors gratefully acknowledge financial support for P.A., F.M., I.P., and M.B. by the Agence Nationale de la Recherche (ANR), for T.W., F.R., J.S., and O.M. by the Deutsche Forschungsgemeinschaft (DFG) via project EC-MEC (ANR-15-CE30-0024-01 and DFG 284207613), for C.Q. and O.M. by the German Federal Ministry of Education and Research (BMBF) via project 05K19FK3, and for M.B., F.F., O.B., and J.L. by the DFG via projects 431791331 (SFB 1452), 214951840 (FOR 1878 funCOS), 453560721, and 431733372. The authors acknowledge the ESRF for the provision of the experimental facilities and thank the staff of ESRF beamlines ID03 and ID31 for technical support. Parts of this research were carried out at beamline P23 of PETRA III at DESY, a member of the Helmholtz Association (HGF). The authors would like to thank D. Novikov and A. Khadiev for their assistance during the experiment. The research leading to this result has been supported by the project CALIPSOplus under the Grant Agreement 730872 from the EU Framework Program for Research and Innovation HORIZON 2020.

## REFERENCES


(1) Dong, Y. M.; He, K.; Yin, L.; Zhang, A. M. A facile route to controlled synthesis of $Co_3O_4$ nanoparticles and their environmental catalytic properties. *Nanotechnology* **2007**, *18*, No. 435602.

(2) Bergmann, A.; Martinez-Moreno, E.; Teschner, D.; Chernev, P.; Gliech, M.; Ferreira de Araujo, J.; Reier, T.; Dau, H.; Strasser, P. Reversible amorphization and the catalytically active state of crystalline $Co_3O_4$ during oxygen evolution. *Nat. Commun.* **2015**, *6*, No. 8625.

(3) Bergmann, A.; Jones, T. E.; Martinez Moreno, E.; Teschner, D.; Chernev, P.; Gliech, M.; Reier, T.; Dau, H.; Strasser, P. Unified structural motifs of the catalytically active state of Co(oxyhydr)oxides during the electrochemical oxygen evolution reaction. *Nat. Cat.* **2018**, *1*, 711−719.

(4) Alvarado, S. R.; Guo, Y. J.; Ruberu, T. P. A.; Bakac, A.; Vela, J. Photochemical versus Thermal Synthesis of Cobalt Oxyhydroxide Nanocrystals. *J. Phys. Chem. C* **2012**, *116*, 10382−10389.

(5) Liu, Y.-C.; Koza, J. A.; Switzer, J. A. Conversion of electrodeposited $Co(OH)_2$ to CoOOH and $Co_3O_4$, and comparison of their catalytic activity for the oxygen evolution reaction. *Electrochim. Acta* **2014**, *140*, 359−365.

(6) Koza, J. A.; He, Z.; Miller, A. S.; Switzer, J. A. Electrodeposition of Crystalline $Co_3O_4$ - A Catalyst for the Oxygen Evolution Reaction. *Chem. Mater.* **2012**, *24*, 3567−3573.

(7) Reikowski, F.; Maroun, F.; Pacheco, I.; Wiegmann, T.; Allongue, P.; Stettner, J.; Magnussen, O. M. Operando Surface X-ray Diffraction Studies of Structurally Defined $Co_3O_4$ and CoOOH Thin Films during Oxygen Evolution. *ACS Catal.* **2019**, *9*, 3811−3821.

(8) Faisal, F.; Stumm, C.; Bertram, M.; Waidhas, F.; Lykhach, Y.; Cherevko, S.; Xiang, F.; Ammon, M.; Vorokhta, M.; Šmíd, B.; Skála, T.; Tsud, N.; Neitzel, A.; Beranová, K.; Prince, K. C.; Geiger, S.; Kasian, O.; Wähler, T.; Schuster, R.; Schneider, M. A.; Matolín, V.; Mayrhofer, K. J. J.; Brummel, O.; Libuda, J. Electrifying model catalysts for understanding electrocatalytic reactions in liquid electrolytes. *Nat. Mater.* **2018**, *17*, 592−598.

(9) Faisal, F.; Bertram, M.; Stumm, C.; Cherevko, S.; Geiger, S.; Kasian, O.; Lykhach, Y.; Lytken, O.; Mayrhofer, K. J. J.; Brummel, O.; Libuda, J. Atomically Defined $Co_3O_4$(111) Thin Films Prepared in Ultrahigh Vacuum: Stability under Electrochemical Conditions. *J. Phys. Chem. C* **2018**, *122*, 7236−7248.

(10) Brummel, O.; Libuda, J. Electrifying Oxide Model Catalysis: Complex Electrodes Based on Atomically-Defined Oxide Films. *Catal. Lett.* **2020**, *150*, 1546−1560.

(11) Buchner, F.; Eckardt, M.; Bohler, T.; Kim, J.; Gerlach, J.; Schnaidt, J.; Behm, R. J. Oxygen Reduction and Evolution on Ni-modified $Co_3O_4$(111) Cathodes for Zn-Air Batteries: A Combined Surface Science and Electrochemical Model Study. *ChemSusChem* **2020**, *13*, 3199−3211.

(12) Boggio, R.; Carugati, A.; Trasatti, S. Electrochemical surface properties of cobalt oxide ($Co_3O_4$) electrodes. *J. Appl. Electrochem.* **1987**, *17*, 828−840.

(13) Potvin, E.; Brossard, L. Oxygen evolution on electrochemically generated cobalt spinel coating. *J. Appl. Electrochem.* **1995**, *25*, 462−471.
(14) Castro, E. B.; Gervasi, C. A.; Vilche, J. R. Oxygen evolution on electrodeposited cobalt oxides. *J. Appl. Electrochem.* **1998**, *28*, 835−841.
(15) Laouini, E.; Hamdani, M.; Pereira, M. I. S.; Douch, J.; Mendonca, M. H.; Berghoute, Y.; Singh, R. N. Electrochemical impedance spectroscopy investigation of spinel type cobalt oxide thin film electrodes in alkaline medium. *J. Appl. Electrochem.* **2008**, *38*, 1485−1494.
(16) Esswein, A. J.; McMurdo, M. J.; Ross, P. N.; Bell, A. T.; Tilley, T. D. Size-Dependent Activity of $Co_3O_4$ Nanoparticle Anodes for Alkaline Water Electrolysis. *J. Phys. Chem. C* **2009**, *113*, 15068−15072.
(17) Hamdani, M.; Singh, R. N.; Chartier, P. $Co_3O_4$ and Co-based spinel oxides bifunctional oxygen electrodes. *Int. J. Electrochem. Sci.* **2010**, *5*, 556−577.
(18) Yeo, B. S.; Bell, A. T. Enhanced activity of gold-supported cobalt oxide for the electrochemical evolution of oxygen. *J. Am. Chem. Soc.* **2011**, *133*, 5587−5593.
(19) Chen, J.; Selloni, A. Water Adsorption and Oxidation at the $Co_3O_4$(110) Surface. *J. Phys. Chem. Lett.* **2012**, *3*, 2808−2814.
(20) García-Mota, M.; Bajdich, M.; Viswanathan, V.; Vojvodic, A.; Bell, A. T.; Noerskov, J. K. Importance of Correlation in Determining Electrocatalytic Oxygen Evolution Activity on Cobalt Oxides. *J. Phys. Chem. C* **2012**, *116*, 21077−21082.
(21) Bajdich, M.; Garcia-Mota, M.; Vojvodic, A.; Noerskov, J. K.; Bell, A. T. Theoretical Investigation of the Activity of Cobalt Oxides for the Electrochemical Oxidation of Water. *J. Am. Chem. Soc.* **2013**, *135*, 13521−13530.
(22) Chen, J.; Selloni, A. First Principles Study of Cobalt (Hydr)oxides under Electrochemical Conditions. *J. Phys. Chem. C* **2013**, *117*, 20002−20006.
(23) Grzelczak, M.; Zhang, J.; Pfrommer, J.; Hartmann, J.; Driess, M.; Antonietti, M.; Wang, X. Electro- and photochemical water oxidation on ligand-free $Co_3O_4$ nanoparticles with tunable sizes. *ACS Catal.* **2013**, *3*, 383−388.
(24) Zhang, M.; de Respinis, M.; Frei, H. Time-resolved observations of water oxidation intermediates on a cobalt oxide nanoparticle catalyst. *Nat. Chem.* **2014**, *6*, 362−367.
(25) Chen, Z.; Kronawitter, C. X.; Koel, B. E. Facet-dependent activity and stability of $Co_3O_4$ nanocrystals towards the oxygen evolution reaction. *Phys. Chem. Chem. Phys.* **2015**, *17*, 29387−29393.
(26) Jeon, H. S.; Jee, M. S.; Kim, H.; Ahn, S. J.; Hwang, Y. J.; Min, B. K. Simple Chemical Solution Deposition of $Co_3O_4$ Thin Film Electrocatalyst for Oxygen Evolution Reaction. *ACS Appl. Mater. Interfaces* **2015**, *7*, 24550−24555.
(27) Leng, X.; Zeng, Q.; Wu, K.-H.; Gentle, I. R.; Wang, D.-W. Reduction-induced surface amorphization enhances the oxygen evolution activity in $Co_3O_4$. *RSC Adv.* **2015**, *5*, 27823−27828.
(28) Plaisance, C. P.; van Santen, R. A. Structure Sensitivity of the Oxygen Evolution Reaction Catalyzed by Cobalt(II,III) Oxide. *J. Am. Chem. Soc.* **2015**, *137*, 14660−14672.
(29) Selcuk, S.; Selloni, A. DFT+U Study of the Surface Structure and Stability of $Co_3O_4$(110): Dependence on U. *J. Phys. Chem. C* **2015**, *119*, 9973−9979.
(30) Tung, C.-W.; Hsu, Y.-Y.; Shen, Y.-P.; Zheng, Y.; Chan, T.-S.; Sheu, H.-S.; Cheng, Y.-C.; Chen, H. M. Reversible adapting layer produces robust single-crystal electrocatalyst for oxygen evolution. *Nat. Commun.* **2015**, *6*, No. 8106.
(31) Xu, Q.-Z.; Su, Y.-Z.; Wu, H.; Cheng, H.; Guo, Y.-P.; Li, N.; Liu, Z.-Q. Effect of Morphology of $Co_3O_4$ for Oxygen Evolution Reaction in Alkaline Water Electrolysis. *Curr. Nanosci.* **2014**, *11*, 107−112.
(32) Zasada, F.; Piskorz, W.; Janas, J.; Grybos, J.; Indyka, P.; Sojka, Z. Reactive Oxygen Species on the (100) Facet of Cobalt Spinel Nanocatalyst and their Relevance in O-16(2)/O-18(2) Isotopic Exchange, deN(2)O, and deCH(4) Processes-A Theoretical and Experimental Account. *ACS Catal.* **2015**, *5*, 6879−6892.
(33) Zasada, F.; Piskorz, W.; Sojka, Z. Cobalt Spinel at Various Redox Conditions: DFT plus U Investigations into the Structure and Surface Thermodynamics of the (100) Facet. *J. Phys. Chem. C* **2015**, *119*, 19180−19191.
(34) Zasada, F.; Piskorz, W.; Janas, J.; Budiyanto, E.; Sojka, Z. Dioxygen Activation Pathways over Cobalt Spinel Nanocubes-From Molecular Mechanism into Ab Initio Thermodynamics and O-16(2)/O-18(2) Exchange Microkinetics. *J. Phys. Chem. C* **2017**, *121*, 24128−24143.
(35) Zasada, F.; Grybos, J.; Piskorz, W.; Sojka, Z. Cobalt Spinel (111) Facets of Various Stoichiometry-DFT plus U and Ab Initio Thermodynamic Investigations. *J. Phys. Chem. C* **2018**, *122*, 2866−2879.
(36) Zhang, P.; Dong, Y.; Kou, Y.; Yang, Z.; Li, Y.; Sun, X. First-Principles Study of Oxygen Evolution Reaction on the Oxygen-Containing Species Covered CoII-Exposing $Co_3O_4$(100) Surface. *Catal. Lett.* **2015**, *145*, 1169−1176.
(37) Zhang, Y.; Ding, F.; Deng, C.; Zhen, S.; Li, X.; Xue, Y.; Yan, Y.-M.; Sun, K. Crystal plane-dependent electrocatalytic activity of $Co_3O_4$ toward oxygen evolution reaction. *Catal. Commun.* **2015**, *67*, 78−82.
(38) Du, S.; Ren, Z.; Qu, Y.; Wu, J.; Xi, W.; Zhu, J.; Fu, H. Co3O4 nanosheets as a high-performance catalyst for oxygen evolution proceeding via a double two-electron process. *Chem. Commun.* **2016**, *52*, 6705−6708.
(39) Pham, H. H.; Cheng, M.-J.; Frei, H.; Wang, L.-W. Surface Proton Hopping and Fast-Kinetics Pathway of Water Oxidation on $Co_3O_4$(001) Surface. *ACS Catal.* **2016**, *6*, 5610−5617.
(40) Plaisance, C. P.; Reuter, K.; van Santen, R. A. Quantum chemistry of the oxygen evolution reaction on cobalt(II,III) oxide - implications for designing the optimal catalyst. *Faraday Discuss.* **2016**, *188*, 199−226.
(41) Wang, H. Y.; Hung, S. F.; Hsu, Y. Y.; Zhang, L. L.; Miao, J. W.; Chan, T. S.; Xiong, Q. H.; Liu, B. In Situ Spectroscopic Identification of mu-OO Bridging on Spinel $Co_3O_4$ Water Oxidation Electrocatalyst. *J. Phys. Chem. Lett.* **2016**, *7*, 4847−4853.
(42) Wang, H.-Y.; Hung, S.-F.; Chen, H.-Y.; Chan, T.-S.; Chen, H. M.; Liu, B. In Operando Identification of Geometrical-Site-Dependent Water Oxidation Activity of Spinel $Co_3O_4$. *J. Am. Chem. Soc.* **2016**, *138*, 36−39.
(43) Zhou, Y.; Dong, C.-K.; Han, L.-L.; Yang, J.; Du, X.-W. Top-Down Preparation of Active Cobalt Oxide Catalyst. *ACS Catal.* **2016**, *6*, 6699−6703.
(44) Amin, H. M. A.; Baltruschat, H. How many surface atoms in $Co_3O_4$ take part in oxygen evolution? Isotope labeling together with differential electrochemical mass spectrometry. *Phys. Chem. Chem. Phys.* **2017**, *19*, 25527−25536.
(45) Favaro, M.; Yang, J.; Nappini, S.; Magnano, E.; Toma, F. M.; Crumlin, E. J.; Yano, J.; Sharp, I. D. Understanding the Oxygen Evolution Reaction Mechanism on CoOx using Operando Ambient-Pressure X-ray Photoelectron Spectroscopy. *J. Am. Chem. Soc.* **2017**, *139*, 8960−8970.
(46) Zhang, R.; Zhang, Y.-C.; Pan, L.; Shen, G.-Q.; Mahmood, N.; Ma, Y.-H.; Shi, Y.; Jia, W.; Wang, L.; Zhang, X.; Xu, W.; Zou, J.-J. Engineering Cobalt Defects in Cobalt Oxide for Highly Efficient Electrocatalytic Oxygen Evolution. *ACS Catal.* **2018**, *8*, 3803−3811.
(47) Lykhach, Y.; Piccinin, S.; Skala, T.; Bertram, M.; Tsud, N.; Brummel, O.; Farnesi Camellone, M.; Beranova, K.; Neitzel, A.; Fabris, S.; Prince, K. C.; Matolin, V.; Libuda, J. Quantitative Analysis of the Oxidation State of Cobalt Oxides by Resonant Photoemission Spectroscopy. *J. Phys. Chem. Lett.* **2019**, *10*, 6129−6136.
(48) Ortiz Peña, N.; Ihiawakrim, D.; Han, M.; Lassalle-Kaiser, B.; Carenco, S.; Sanchez, C.; Laberty-Robert, C.; Portehault, D.; Ersen, O. Morphological and Structural Evolution of $Co_3O_4$ Nanoparticles Revealed by in Situ Electrochemical Transmission Electron Microscopy during Electrocatalytic Water Oxidation. *ACS Nano* **2019**, *13*, 11372−11381.
(49) Bergmann, A.; Roldan Cuenya, B. Operando Insights into Nanoparticle Transformations during Catalysis. *ACS Catal.* **2019**, *9*, 10020−10043.


https://doi.org/10.1021/acscatal.1c05169
*ACS Catal.* 2022, 12, 3256−3268

(50) Jiang, H.; He, Q.; Zhang, Y.; Song, L. Structural Self-Reconstruction of Catalysts in Electrocatalysis. *Acc. Chem. Res.* **2018**, *51*, 2968−2977.
(51) Gao, L.; Cui, X.; Sewell, C. D.; Li, J.; Lin, Z. Recent advances in activating surface reconstruction for the high-efficiency oxygen evolution reaction. *Chem. Soc. Rev.* **2021**, *50*, 8428−8469.
(52) Burke, M. S.; Enman, L. J.; Batchellor, A. S.; Zou, S.; Boettcher, S. W. Oxygen Evolution Reaction Electrocatalysis on Transition Metal Oxides and (Oxy)hydroxides: Activity Trends and Design Principles. *Chem. Mater.* **2015**, *27*, 7549−7558.
(53) Moysiadou, A.; Lee, S.; Hsu, C. S.; Chen, H. M.; Hu, X. L. Mechanism of Oxygen Evolution Catalyzed by Cobalt Oxyhydroxide: Cobalt Superoxide Species as a Key Intermediate and Dioxygen Release as a Rate-Determining Step. *J. Am. Chem. Soc.* **2020**, *142*, 11901−11914.
(54) Zasada, F.; Janas, J.; Piskorz, W.; Sojka, Z. Surface oxygen dynamics and H-2 oxidation on cobalt spinel surface probed by O-18/O-16 isotopic exchange and accounted for by DFT molecular modeling: facile interfacial oxygen atoms flipping through transient peroxy intermediate. *Res. Chem. Intermed.* **2017**, *43*, 2865−2880.
(55) Meng, J.; Cui, Z.; Yang, X.; Zhu, S.; Li, Z.; Qi, K.; Zheng, L.; Liang, Y. Cobalt-iron (oxides) water oxidation catalysts: Tracking catalyst redox states and reaction dynamic mechanism. *J. Catal.* **2018**, *365*, 227−237.
(56) Curutchet, A.; Colinet, P.; Michel, C.; Steinmann, S. N.; Le Bahers, T. Two-sites are better than one: revisiting the OER mechanism on CoOOH by DFT with electrode polarization. *Phys. Chem. Chem. Phys.* **2020**, *22*, 7031−7038.
(57) Surendranath, Y.; Kanan, M. W.; Nocera, D. G. Mechanistic Studies of the Oxygen Evolution Reaction by a Cobalt-Phosphate Catalyst at Neutral pH. *J. Am. Chem. Soc.* **2010**, *132*, 16501−16509.
(58) Jiao, F.; Frei, H. Nanostructured Cobalt Oxide Clusters in Mesoporous Silica as Efficient Oxygen-Evolving Catalysts. *Angew. Chem., Int. Ed.* **2009**, *48*, 1841−1844.
(59) Meyer, W.; Biedermann, K.; Gubo, M.; Hammer, L.; Heinz, K. Surface structure of polar $Co_3O_4$(111) films grown epitaxially on Ir(100)-(1 ×1). *J. Phys.: Condens. Matter* **2008**, *20*, No. 265011.
(60) Biedermann, K.; Gubo, M.; Hammer, L.; Heinz, K. Phases and phase transitions of hexagonal cobalt oxide films on Ir(100)-(1 ×1). *J. Phys.: Condens. Matter* **2009**, *21*, No. 185003.
(61) Magnussen, O. M.; Krug, K.; Ayyad, A. H.; Stettner, J. In situ diffraction studies of electrode surface structure during gold electrodeposition. *Electrochim. Acta* **2008**, *53*, 3449−3458.
(62) Burke, M. S.; Kast, M. G.; Trotochaud, L.; Smith, A. M.; Boettcher, S. W. Cobalt-Iron (Oxy)hydroxide Oxygen Evolution Electrocatalysts: The Role of Structure and Composition on Activity, Stability, and Mechanism. *J. Am. Chem. Soc.* **2015**, *137*, 3638−3648.
(63) Gerken, J. B.; McAlpin, J. G.; Chen, J. Y. C.; Rigsby, M. L.; Casey, W. H.; Britt, R. D.; Stahl, S. S. Electrochemical Water Oxidation with Cobalt-Based Electrocatalysts from pH 0-14: The Thermodynamic Basis for Catalyst Structure, Stability, and Activity. *J. Am. Chem. Soc.* **2011**, *133*, 14431−14442.
(64) Behl, W. K.; Toni, J. E. Anodic Oxidation of Cobalt in Potassium Hydroxide Electrolytes. *J. Electroanal. Chem.* **1971**, *31*, 63.
(65) Grumelli, D.; Wiegmann, T.; Barja, S.; Reikowski, F.; Maroun, F.; Allongue, P.; Balajka, J.; Parkinson, G. S.; Diebold, U.; Kern, K.; Magnussen, O. M. Electrochemical Stability of the Reconstructed $Fe_3O_4$(001) Surface. *Angew. Chem., Int. Ed.* **2020**, *59*, 21904−21908.
(66) Hrkac, S. B.; Koops, C. T.; Abes, M.; Krywka, C.; Muller, M.; Burghammer, M.; Sztucki, M.; Dane, T.; Kaps, S.; Mishra, Y. K.; Adelung, R.; Schmalz, J.; Gerken, M.; Lage, E.; Kirchhof, C.; Quandt, E.; Magnussen, O. M.; Murphy, B. M. Tunable Strain in Magneto-electric ZnO Microrod Composite Interfaces. *ACS Appl. Mater. Interfaces* **2017**, *9*, 25571−25577.
(67) Damjanovic, A.; Dey, A.; Bockris, J. O. M. Kinetics of oxygen evolution and dissolution on platinum electrodes. *Electrochim. Acta* **1966**, *11*, 791−814.
(68) Bockris, J. O. M.; Otagawa, T. The Electrocatalysis of Oxygen Evolution on Perovskites. *J. Electrochem. Soc.* **1984**, *131*, 290−302.
(69) Wade, W. H.; Hackerman, N. Anodic Phenomena at an Iron Electrode. *Trans. Faraday Soc.* **1957**, *53*, 1636−1647.
(70) Ullman, A. M.; Brodsky, C. N.; Li, N.; Zheng, S.-L.; Nocera, D. G. Probing Edge Site Reactivity of Oxidic Cobalt Water Oxidation Catalysts. *J. Am. Chem. Soc.* **2016**, *138*, 4229−4236.
(71) Wang, J. S.; Liu, J.; Zhang, B.; Wan, H. Z.; Li, Z. S.; Ji, X.; Xu, K.; Chen, C.; Zha, D.; Miao, L.; Jiang, J. J. Synergistic effect of two actions sites on cobalt oxides towards electrochemical water-oxidation. *Nano Energy* **2017**, *42*, 98−105.


https://doi.org/10.1021/acscatal.1c05169
*ACS Catal.* 2022, 12, 3256−3268